Paramagnetic defects induced by electron irradiation in barium hollandite ceramics for caesium storage

2006 J. Phys.: Condens. Matter 18 4007

(http://iopscience.iop.org/0953-8984/18/16/009)

INSTITUTE OF PHYSICS PUBLISHING JOURNAL OF PHYSICS: CONDENSED MATTER

J. Phys.: Condens. Matter **18** (2006) 4007–4027 doi:10.1088/0953-8984/18/16/009

Paramagnetic defects induced by electron irradiation in barium hollandite ceramics for caesium storage

V Aubin-Chevaldonnet[1], D Gourier[1], D Caurant[1], S Esnouf[2], T Charpentier[3] and J M Costantini[4]

[1] CNRS, Ecole Nationale Supérieure de Chimie de Paris (ENSCP, ParisTech), Laboratoire de Chimie de la Matière Condensée de Paris, UMR-CNRS 7574, 11, rue P et M Curie, 75231 Paris Cedex 05, France
[2] Ecole Polytechnique (ParisTech) and Commissariat à l'Energie Atomique CEA/DSM/DRECAM, Laboratoire des solides irradiés, 91128 Palaiseau, France
[3] Commissariat à l'Energie Atomique CEA/DSM/DRECAM/SCM, CEA-CNRS URA 331, 91191 Gif sur Yvette, France
[4] Commissariat à l'Energie Atomique CEA/DEN/DMN, Service de Recherche en Métallurgie Appliquée, 91191 Gif sur Yvette, France

E-mail: didier-gourier@enscp.fr

Received 10 January 2006, in final form 14 March 2006
Published 7 April 2006
Online at stacks.iop.org/JPhysCM/18/4007

Abstract

We have studied by electron paramagnetic resonance the mechanism of defect production by electron irradiation in barium hollandite, a material used for immobilization of radioactive caesium. The irradiation conditions were the closest possible to those occurring in Cs storage waste forms. Three paramagnetic defects were observed, independently of the irradiation conditions. A hole centre (H centre) is attributed to a superoxide ion O_2^- originating from hole trapping by interstitial oxygen produced by electron irradiation. An electron centre (E_1 centre) is attributed to a Ti^{3+} ion adjacent to the resulting oxygen vacancy. Another electron centre (E_2 centre) is attributed to a Ti^{3+} ion in a cation site adjacent to an extra Ba^{2+} ion in a neighbouring tunnel, originating from barium displacement by elastic collisions. Comparison of the effects of external irradiations by electrons with the β-decay of Cs in storage waste forms is discussed. It is concluded that the latter would be dominated by E_1 and H centres rather than E_2 centres.

(Some figures in this article are in colour only in the electronic version)

1. Introduction

Highly durable specific host phases for long-lived fission product immobilization are currently under study for enhanced reprocessed high level nuclear wastes [1, 2]. Among these wastes, caesium appears to be one of the most difficult radionuclides to immobilize because of the high activities of ^{134}Cs (half-life of 2 years) and ^{137}Cs (half-life of 30 years) isotopes and the

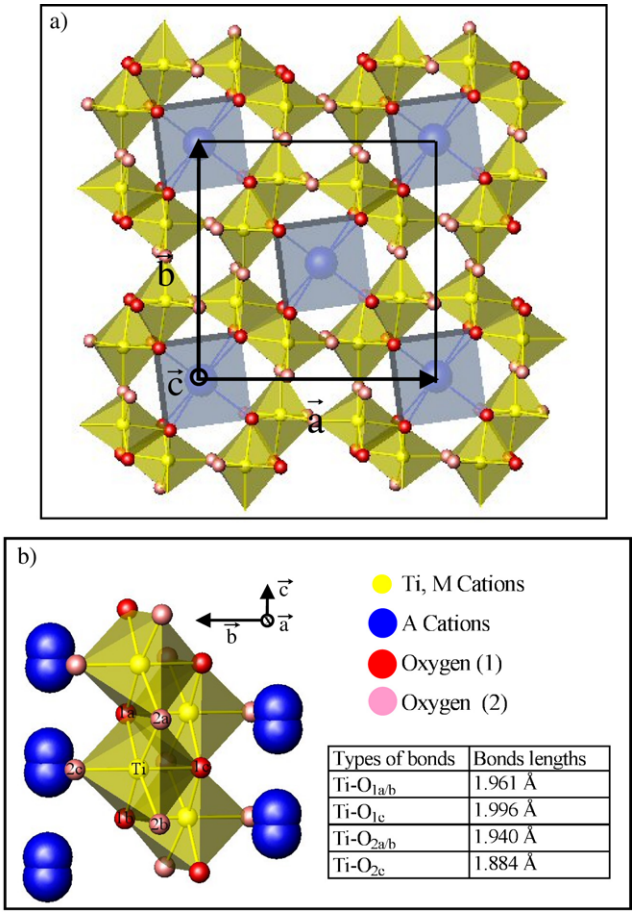

Figure 1. (a) Projection along the **c**-axis of the tetragonal ($I4/m$) hollandite-type $A_z(Ti, M)_8O_{16}$ structure. Edge-sharing and corner-sharing $[Ti, M]O_6$ octahedra form square tunnels in the **c**-direction. The large A cations (and vacancies) are located in box-shaped cavities of the tunnels. The two kinds of oxygen (O_1 and O_2) are also indicated. (b) Rutile-like strings of $[Ti, M]O_6$ octahedra along **c**-axis. The two possible off-centre equilibrium positions of A cations within the box-shaped cavities are shown. Obviously these two positions cannot be occupied simultaneously.

occurrence of nearly 14% of the long-lifetime ^{135}Cs isotope (half-life of 2.3×10^6 years). The decay of the caesium radioactive isotopes involves the emission of β^- particles with energy E ranging from 0.089 to 1.454 MeV, γ rays (0.475 MeV $\leqslant E \leqslant$ 1.168 MeV) and the transmutation of Cs to stable Ba:$Cs^+ \rightarrow Ba^{2+} + e^-(\beta) + \gamma$ [3, 4]. Therefore, Cs-host forms must be stable under (β, γ)-irradiation and must accommodate the valence and ionic radius changes resulting from Cs decay.

(Ba, Cs) hollandite ceramics, nominally $[Ba^{2+}{}_xCs^+{}_y][M^{3+}_{2x+y}Ti^{4+}_{8-2x-y}O_{16}]$ $(x + y < 2)$, with M being trivalent cations such as Ti^{3+}, Fe^{3+}, and Al^{3+}, appeared to be one of the best candidates for the specific immobilization of caesium. Indeed, this host phase is able to accommodate chemistry and valence changes due to the caesium decay because of the high capacity of hollandite to incorporate Ba, the charge compensation being ensured by the reduction of a fraction of Ti^{4+} ions [5]. The titanate hollandite $A_z(Ti, M)_8O_{16}$ (with A = Ba^{2+} and Cs^+, $z \leqslant 2$) type structure is shown in figure 1. Square tunnels are enclosed by columns of

two edge-sharing octahedra, which share corners to form tunnels running parallel to the short axis of the structure. The small Ti and M cations are located in the octahedral sites that form strings as in the rutile structure [6]. The large cations Ba^{2+} and Cs^{+} are set in the tunnels in box-shaped cavities of eight oxygen ions. The cell symmetry may be tetragonal ($I4/m$ space group) or monoclinic ($I2/m$ space group), depending generally on the mean ratio of cation radii $R_A/R_{B,M}$ of the A and (B, M) cations [7]. The trivalent M cations in octahedra ensured the charge compensation due to the excess of positive charge in the tunnels. A maximum of two A cations per unit formula (i.e. $z = 2$) can be incorporated in the hollandite structure. However, the tunnels are only partially occupied ($z < 2$) in Ba hollandite, and A cations and vacant sites may take up an ordered arrangement along the tunnels (superlattice ordering), depending on the hollandite composition [7, 8]. In spite of the relatively open-framework-type structure of (Ba, Cs) hollandite, the Ba^{2+} and Cs^{+} ions have to overcome a large energy barrier associated with passing through the square planar arrangement of oxygen ions to migrate along the axis of the tunnels. Thus, these large cations are well immobilized.

Due to the lack of natural analogues containing radioactive caesium, the radiation resistance of (Ba, Cs) hollandite has not been proved as yet. Moreover, to the best of our knowledge, the incorporation and the study of the effects of radioactive caesium in synthetic single-phase hollandite has not been already performed. Finally, literature reports only external irradiation experiments that are not relevant to simulate the effects of caesium decay on hollandite long-term behaviour [9–14]. The few works dealing with the stability of single-phase (Ba, Cs) hollandite under external electron irradiation, used to simulate β-irradiation of caesium, were performed with intense electron irradiation in transmission electron microscopes. In this case, strong structural evolutions were observed such as the hollandite $\rightarrow$ rutile transformation [9] by loss of tunnel cations, and microtwinning followed by amorphization [10]. However, it must be underlined that the electron dose rate caused by β self-irradiation in the radioactive Cs waste forms will be low in comparison with the electron dose rate received in the electron microscope. Thus the latter overestimates the real effects of Cs decay [9, 10].

To the best of our knowledge, no studies concerning point defects induced by β or γ irradiations of hollandite have ever been reported in the literature. On the basis of electron paramagnetic resonance (EPR) and ^{27}Al magic angle nuclear magnetic resonance (MAS-NMR) spectroscopies, we studied in this work the nature and the mechanism of formation of defects produced by external electron irradiation experiments simulating Cs β-decay. Because of the complexity of the hollandite structure, it is not possible to extrapolate mechanisms and defects found for simple oxides such as MgO, CaO, Al_2O_3 or ZrO_2 for example. In this paper, one Ba hollandite $Ba_{1.16}Al_{2.32}Ti_{5.68}O_{16}$ composition was selected, which is close to the lower bound ($1.14 \leqslant x \leqslant 1.23$) of the compositional range of Ba hollandite with $M = Al^{3+}$ prepared under air [15], with a view to inserting caesium more easily. Ceramic samples and single crystals were prepared by an oxide route [16] and by a flux method [17], respectively. In order to optimize the detection of paramagnetic defects, we did not study hollandites containing high numbers of native paramagnetic ions ($M = Ti^{3+}$, Fe^{3+}) that are used to optimize Cs incorporation in the structure [18, 19]. External electron irradiations (1.0–2.5 MeV) with a Van de Graaff accelerator were used to simulate the β particles and Compton electrons generated by γ rays emitted by radioactive caesium.

Preliminary results have been reported elsewhere [20]. Three paramagnetic defects are observed in this work. A hole centre (H centre) is attributed to a superoxide ion O_2^- originating from hole trapping by interstitial oxygen produced by electron irradiation. An electron centre (E_1 centre) is attributed to a Ti^{3+} ion adjacent to the resulting oxygen vacancy. Another electron centre (E_2 centre) is attributed to a Ti^{3+} ion in a cation site adjacent to an extra Ba^{2+} ion

in a neighbouring tunnel, originating from barium displacement by elastic collisions. The mechanism of formation of these defects is discussed, and comparison of the effects of external electron irradiations with the β-decay of Cs in storage waste forms indicates that defects in waste forms would be dominated by E_1 and H centres rather than E_2 centres.

2. Experimental details

2.1. Synthesis and characterizations of hollandite ceramics and single crystals

$Ba_{1.16}Al_{2.32}Ti_{5.68}O_{16}$ hollandite ceramics were prepared by solid-state reaction from oxides and carbonates (Al_2O_3, TiO_2 and $BaCO_3$) [17]. Reagent powders (almost 10 g) were mixed and ground with an agate mortar, pelletized and calcined under air for 4 h at 810 °C. Once ground again and pelletized, the calcined powders were sintered at 1320 °C for 96 h. The resulting ceramics were almost single phases as shown by x-ray diffraction (XRD), except a few traces of an unidentified parasitic phase containing mainly barium and phosphorus as observed by scanning electron microscopy (SEM) and energy dispersive x-ray analysis (EDX). This phase resulted from phosphorus impurities in raw materials and can be avoided using phosphate-free rutile. Moreover, the composition $Ba_{1.17}Al_{2.28}Ti_{5.71}O_{16}$, determined by electron probe microanalysis (EPMA), was very close to the expected one. The crystal structure of the ceramics is tetragonal ($I4/m$) with cell parameters $a = b = 9.969$ Å and $c = 2.923$ Å. They were relatively dense ($\approx$3.86 g cm^{-3}), which represents 90% of the theoretical density (4.29) determined from lattice parameters.

Hollandite single crystals were also synthesized by the slow cooling flux method to identify more precisely the irradiation-induced defects detected by EPR. They were grown by dissolving the mixture of oxides and carbonate (Al_2O_3, TiO_2 and $BaCO_3$) in stoichiometric proportions corresponding to $Ba_{1.16}Al_{2.32}Ti_{5.68}O_{16}$ in a flux of $(BaF_2)_{0.47}(B_2O_3)_{0.53}$ composition. The best flux/hollandite ratio was 60/40 wt% [17]. The reagents (almost 80 g) were heated in air in a platinum crucible (1400 °C) and slowly cooled (3 °C h^{-1}) from 1400 to 900 °C. The crystals were removed from the crucible by dissolving the flux in hot acidic water. The hollandite single crystals showed an acicular shape (7 mm length and 1 mm width) with their elongated direction along the c-axis of the tetragonal structure. Their natural faces were of {110} and {100} type as shown by XRD, the latter being less developed than the former. Their composition was $Ba_{1.23}Al_{2.04}Ti_{5.85}O_{16}$ as determined by EPMA, which is close to the ceramic composition.

2.2. Irradiation of hollandite samples

To evaluate the stability of hollandite ceramics and single crystals under β and γ irradiations of radioactive caesium, 0.5–1 mm thick samples were irradiated at almost room temperature ($T < 50$ °C) using 1.0, 1.5 and 2.5 MeV electrons generated by a Van de Graaff accelerator. These electron irradiations simulate not only the β particles emitted by radioactive caesium but also the Compton electrons resulting from the absorption of caesium γ rays by hollandite samples. Indeed, considering the average energy of γ rays (around 0.6 MeV) emitted by caesium in the hollandite composition studied here, the Compton effect dominates the γ ray–matter interaction [21]. The samples were subjected to different electron fluences (number of incident electrons per cm^2) between 3.4×10^{17} cm^{-2} and 1.2×10^{19} cm^{-2} with 1.0–2.5 MeV electron energies, giving absorbed doses in the 1.4×10^8–7.5×10^9 Gy range. The influence of these irradiation conditions on the nature and the concentration of point defects were thus estimated.

The PENELOPE software [22] was used to quantify the fluences and absorbed doses during the electron irradiations. It allowed us to reproduce exactly the experimental setting,

i.e. layers of different materials (copper/hollandite/copper) introduced in the Van de Graaff accelerator. The fraction of absorbed electrons and the energies per incident particle deposited in our samples were thus estimated. Cross sections of the different atoms and the number of atomic displacements per atom were calculated by using a computer code developed by Lesueur *et al* [23, 24].

2.3. Magnetic resonance

As electron irradiations imply mainly ionizations and electronic excitations (electron–hole pair production) in materials, the formation of paramagnetic point defects is expected in hollandite. In order to foresee the nature of these defects we performed semi-empirical calculation of the hollandite electronic band structure using an extended Hückel tight-binding (EHTB) method [17]. This showed that the top of the valence band and the bottom of the conduction band are mainly constituted of oxygen 2p orbitals and titanium 3d orbitals, respectively. Therefore, it is expected that electron centres would be Ti^{3+} ions (after electron trapping by Ti^{4+} ions) and hole centres would be of O^- or O_2^{n-} ($n < 4$) type (after hole(s) trapping by oxygen ions).

EPR experiments were carried out on both pristine and irradiated samples using Bruker ESP 300e and ELEXYS E500 spectrometers operating at the X band (9.5 GHz) in the range of temperature 9–300 K. The EPR signals were simulated using the software SIMFONIA developed by *Bruker Biospin* in order to extract their g factors. The spin concentrations corresponding to the different EPR signals were determined by comparison with the spectrum of a standard DPPH (1,1 diphenyl-2picrylhydrazyl) sample containing 1.0066×10^{17} spins. The spin quantifications of hole centre signals resulted directly from the double integration of the experimental EPR signals whereas the double integration was performed on the individual simulated spectra for electron centres because of a significant overlapping between several different signals. These electron centre signals were recorded at different temperatures (10 or 70 K) to play with the saturation effects and lifetime broadening to separate and identify the different defects.

Solid-state ^{27}Al MAS NMR (magic angle spinning nuclear magnetic resonance) spectra of pristine and irradiated samples were collected on a Bruker AVANCE 500 (11.7 T) spectrometer operating at a Larmor frequency of 130.066 MHz. 2.5 mm o.d. (for ^{27}Al) commercial Bruker MAS probes were used and the sample-spinning speed was set to 31.25 kHz. The ^{27}Al chemical shifts are reported in ppm relative to an external sample of 1.0 M $AlCl_3{\cdot}6H_2O$. MAS spectra were acquired using a recycle delay of 1 s and a $\pi/12$ pulse. Triple quantum MQMAS spectra were acquired using a Z-filter sequence [25] and a recycle delay of 1 s.

3. Results

3.1. Paramagnetic defects in pristine samples

Pristine hollandite ceramics often exhibit EPR signals due to two types of defects, namely paramagnetic transition metal ions such as Fe^{3+}, Cu^{2+} and V^{4+} present in the raw materials used for the synthesis, and Ti^{3+} due to partial reduction of Ti^{4+} ions of the bulk material. Fe^{3+} impurities (100–420 ppm), represented by a distorted EPR line at $g = 4.3$, are localized in octahedral sites of Al^{3+} and Ti^{3+}. The presence of this signal, which is very different from that of iron in rutile [26, 27], shows that the hollandite ceramics do not contain rutile as secondary phase. Typical EPR spectra of Cu^{2+} (200 ppm) and V^{4+} impurities (about 1000 ppm) are also easily observed at low temperature (below 100 K). As these EPR lines appear in the magnetic

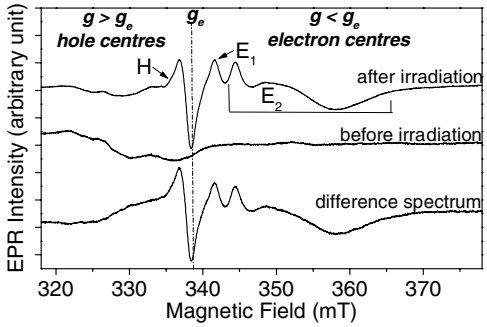

Figure 2. Typical X-band EPR spectra at $T = 70$ K of hollandite ceramics before and after 1.0 MeV electron irradiation (fluence 1.4×10^{19} cm^{-2}) and their difference spectrum. The free electron g factor is indicated to differentiate hole and electron centres.

field range of irradiation induced defects, they always contribute to the total EPR spectrum and must be taken into account in the interpretation of spectra.

A signal of Ti^{3+} (referred to as the E_0 centre) is often observed at very low temperature (typically 10 K) and at concentration in the range 3×10^{15}–10^{16} cm^{-3}. The fact that this signal is detected only at very low temperature indicates that this Ti^{3+} is localized in an undistorted octahedral site of the hollandite structure (see below). In order to avoid overlapping with irradiation induced Ti^{3+} centres, we selected samples containing no E_0 centres.

3.2. Paramagnetic defects induced by electron irradiation

White hollandite ceramics take a pronounced colour upon electron irradiation, which varies from yellow-brown to dark brown for electron fluence between 10^{17} and 10^{19} cm^{-2}, indicating that colour centres are formed. EPR shows that a significant fraction of these colour centres are paramagnetic. Figure 2 shows a general view of the EPR spectrum recorded at 70 K before and after irradiation with 1 MeV electrons at fluence 1.4×10^{19} cm^{-2}. The vertical line represents the magnetic field corresponding to the free spin value $g_e = 2.0023$, which is the boundary between hole centres ($g > g_e$) and electron centres ($g < g_e$). As paramagnetic impurities give broad features at $g > g_e$ for Cu^{2+}, and in a broad magnetic field range for V^{4+}, the effect of irradiation can be studied after subtracting the spectrum of the pristine sample from that recorded after irradiation. As shown below, the lines in the $g < g_e$ region represent irradiation induced Ti^{3+} centres, while the broad signal at $g > g_e$ represents hole centres. However a fine analysis of the spectra outside the magnetic field range of irradiation induced centres, where EPR lines of V^{4+}, Cu^{2+} and Fe^{3+} are well identified, shows a decrease of intensity of these lines after irradiation. This indicates that these impurities are partially reduced (Fe^{2+}, Cu^{+}, V^{3+}) or oxidized (V^{5+}) upon electron irradiation. To account for this modification of the background EPR intensity, the baseline subtractions in figure 2 were made by adjusting the intensity of well identified lines of Cu^{2+} or V^{4+} before and after irradiation.

As the EPR spectrum of irradiated hollandite exhibits several partially overlapping lines, their attribution to specific defects cannot be made with only one spectrum. The spectrum of each species has been identified by monitoring the evolution of the EPR lineshape and intensity upon variation of different experimental parameters, such as temperature, incident microwave power, electron energy and fluence.

The spectrum labelled H in figure 2 represents one type of paramagnetic centre, as its shape does not vary, except the intensity, upon variation of temperature and microwave power.

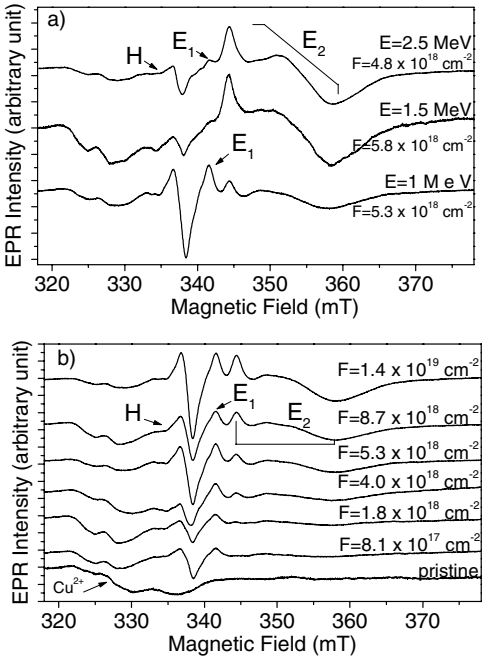

Figure 3. Influence of the electron energy (a) and fluence of 1.0 MeV electrons (b) on the relative proportions of the EPR signals. Energy E of electrons and fluence F are indicated near the spectra. Temperature $T = 70$ K.

In contrast, the EPR signal in the region $g < g_e$ represents two different paramagnetic centres, referred to as E_1 and E_2 centres. The E_1 centre is represented by a single line, and is detectable up to room temperature. The broad multicomponent signal of the E_2 centre vanishes above 140–170 K, depending on the samples, so that only the E_1 centre is observable at higher temperature. The E_2 spectrum readily saturates at very low temperature (10 K), in contrast to the E_1 centre, so that the latter is also easily observed at low temperature and high microwave power.

Figure 3 shows the EPR spectra at 70 K at different electron energies (figure 3(a)) and fluences at 1 MeV electron energy (figure 3(b)). It should be noted that the spectra of figure 3 have not been corrected by baseline subtraction, so that the low magnetic field parts of the spectra represent the variation of both H centres and Cu^{2+}, V^{4+} impurities. However, all these spectra show that the same H, E_1 and E_2 centres are always produced whatever the irradiation conditions. Only their relative proportions depend on electron energy and fluence. The ratio E_2/E_1 increases and the ratio $H/(E_1+E_2)$ decreases upon increasing electron energy at constant fluence (figure 3(a)). In particular, the E_2 centre dominates the EPR spectrum at 1.5 and 2.5 MeV. As shown below, this energy dependence of the E_2 intensity suggests that this centre is related to atomic displacements upon electron irradiation. The total intensity increases with the fluence at fixed electron energy (figure 3(b)); however, the intensity of E_2 and E_1 centres increases more rapidly than that of the H centre (i.e. $H/(E_1 + E_2)$ decreases).

4. Identification of paramagnetic centres

4.1. H centres

Figure 4 shows an expanded view of the experimental and simulated spectra of the H centre, the former being corrected by baseline subtraction. The spectrum can be simulated by the

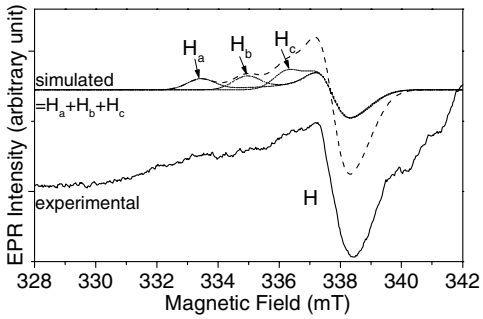

Figure 4. Simulation of the EPR signal of the H centre. Samples were irradiated by 2.5 MeV electrons at a fluence of 4.8×10^{18} cm^{-2}. Temperature $T = 70$ K. Three components H_a, H_b and H_c are required to reproduce the H signal.

Table 1. The main characteristics of irradiation-induced centres H, E_1 and E_2: the maximum temperature $T_{detection}$ above which the signal is not detectable, the g factors (g_1, g_2, g_3) and corresponding linewidth ΔB determined after the simulation of all EPR signals using Gaussian lineshapes. Three components H_a, H_b and H_c representing three variants of the H centre are necessary to reproduce this signal.

Signals	Samples	$T_{detection}$ (K)		g factor	Linewidth ΔB (mT)
H	Polycrystalline	298	H_a component	$g_1 = 2.0038$	1.2
				$g_2 = 2.009$	0.8
				$g_3 = 2.035$	0.9
			H_b component	$g_1 = 2.0038$	1.2
				$g_2 = 2.009$	0.8
				$g_3 = 2.026$	0.9
			H_c component	$g_1 = 2.0038$	1.2
				$g_2 = 2.009$	0.8
				$g_3 = 2.018$	0.9
E_1	Polycrystalline	298	Simulation SA	$g_1 = 1.981$	1.5
				$g_2 = 1.972$	3
				$g_3 = 1.953$	3
			Simulation SB	$g_1 = 1.963$	4.2
				$g_2 = 1.909$	4.2
				$g_3 = 1.882$	1.4
E_2	Polycrystalline	170		$g_\perp = 1.898$	7
				$g_\parallel = 1.965$	1.5
	Single crystal	190		$g_1 = 1.888$	4.75
				$g_2 = 1.886$	4.75
				$g_3 = g_c = 1.965$	1.87

superposition of at least three powder spectra representing three centres of the same type, referred to as H_a, H_b and H_c centres. Gaussian lineshape functions were used in all cases. Indeed, we observed that the shape of the low magnetic field tail of the spectrum slightly differ from sample to sample, which is an indication of the complexity of this defect. Parameters of the simulations are given in table 1. The H centres are characterized by rhombic g factors with three components, among which two components ($g_1 = 2.0038$ and $g_2 = 2.009$) are

common to the three H centres. They differ by the third g component, which amounts to $g_3 = 2.035, 2.026$ and 2.018 for H_a, H_b and H_c centres, respectively. These parameters are in the range classically found for oxygen centres in oxides, characterized by a hole trapped in filled 2p orbitals of oxygen [28]. If the hole is localized in a σ-type molecular orbital containing $2p_z$ oxygen orbitals, we expect no spin–orbit effect along the z axis of the centre, and g factors are given by [28]

$$\begin{aligned} g_{\parallel} &= g_e \\ g_{\perp} &= g_e - \frac{2\lambda}{\Delta} \end{aligned} \tag{1}$$

where $g_e = 2.0023$ and $\lambda = -0.017$ eV are the free electron g value and the spin–orbit coupling constant of the O^- ion, respectively. Expression (1) gives a sequence $g_{\perp} > g_{\parallel} \approx 2.002$. This situation corresponds to O^- ion stabilized by an adjacent cationic defect, which creates the energy splitting Δ. In this case the hole is trapped in the $2p_z$ oxygen orbital pointing towards the cationic defect [28]. This situation is also found with O_2^{3-} centres with configuration $(\ldots 1\pi_u)^4$, $(1\pi_g^*)^4$, $(3\sigma_u^*)^1$, originating from the trapping of a O^- centre by a lattice O^{2-} ion (see figure 12 for the energy level diagram). In both cases the g anisotropy is mainly determined by the axial component of the crystal field, producing the splitting between $\sigma_u(2p_z)$ and $\pi_g(2p_x, 2p_y)$ manifolds. In contrast, if the hole is localized in a π-type molecular orbital made of $2p_x$, $2p_y$ oxygen orbitals, such as is the case for superoxide O_2^- centres with configuration $(\ldots 1\pi_u)^4$, $(1\pi_g^*)^3$, $(3\sigma_u^*)^0$ (see figure 12), we expect g factors given by the following expression [29]:

$$\begin{aligned} g_y &= \frac{g_e\delta}{(\delta^2+\lambda^2)^{1/2}} + \frac{\lambda}{\Delta}\left[\frac{\delta+\lambda}{(\delta^2+\lambda^2)^{1/2}} - 1\right] \\ g_x &= \frac{g_e\delta}{(\delta^2+\lambda^2)^{1/2}} + \frac{\lambda}{\Delta}\left[\frac{\delta-\lambda}{(\delta^2+\lambda^2)^{1/2}} + 1\right] \\ g_z &= g_e + \frac{2\lambda}{(\delta^2+\lambda^2)^{1/2}} \end{aligned} \tag{2}$$

where $\lambda = 0.014$ eV is the spin–orbit coupling constant of O_2^- [30], Δ is the splitting between the ground state bonding σ_g orbital and the antibonding π_g^* orbital containing the unpaired electron, and δ is the splitting of the π_g^* manifold. In the case of a pure axial symmetry ($\delta = 0$ in equation (2)) we expect $g_z = 4$ and $g_x = g_y = 0$. In contrast, when the O_2^- ion is trapped in a solid, the non-axial crystal field component splits the π_g^* manifold, and equation (2) gives g factors closer to two for $\delta \gg \lambda$, with a g-factor order $g_z > g_x > g_y \approx 2.0023$:

$$\begin{aligned} g_y &= g_e \\ g_x &= g_e + \frac{2\lambda}{\Delta} \\ g_z &= g_e + \frac{2\lambda}{\delta}. \end{aligned} \tag{3}$$

Moreover, as the g_z factor is mainly determined by a non-axial crystal field, it is very sensitive to the surrounding of O_2^- centre [30]. From equation (3), the g_z values (g_3 values in table 1) of H_a, H_b and H_c centres correspond to a splitting δ of the antibonding π_g^* manifold equal to 0.86, 1.18 and 1.78 eV, respectively.

The g factors found for H centres agree with the known characteristics of superoxide O_2^- centres, with the g_z values corresponding to three different sites of the O_2^- centre in the hollandite structure. For example, the values $g_z = g_3 = 2.035$, $g_x = g_2 = 2.009$ and $g_y = g_1 = 2.0038$ of the H_a centre in hollandite are close to the values $g_z = 2.030$, $g_x = 2.008$

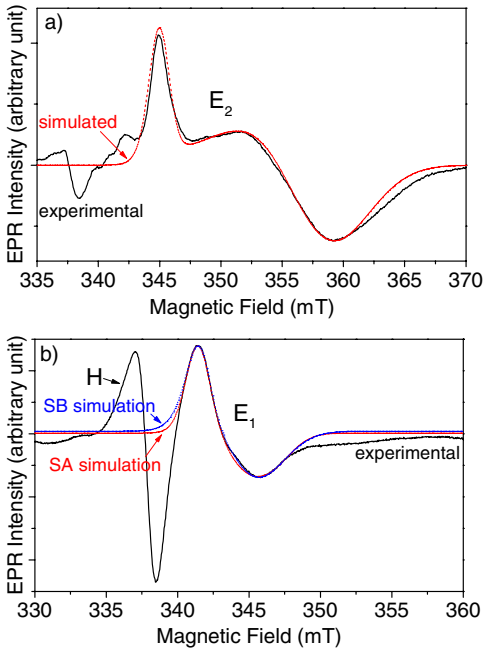

Figure 5. (a) Simulation of E_2 signal on samples irradiated by 2.5 MeV electrons at a fluence of 4.8×10^{18} cm^{-2} recorded at $T = 70$ K. (b) Two possible simulations of E_1 signal on samples irradiated by 1.0 MeV electrons at a fluence of 1.4×10^{19} cm^{-2} and recorded at $T = 10$ K.

and $g_y = 2.004$ found for O_2^- centres in rutile [31]. Other values found for O_2^- in rutile ($g_z = 2.0243$, $g_x = 2.0095$ and $g_y = 2.0036$) [32] are very close to the values found in this work for the H_b centre. In contrast, the sequence of g factors of H centres is significantly different from what is known for O^- and O_2^{3-} centres in oxides, so we may conclude from this analysis that the main hole centres produced by electron irradiation in hollandite are superoxide O_2^- ions in different types of environments.

The origin of the difference between the three H centres is more difficult to explain. However it has been shown that the g_z parameter decreases (δ increases) when the charge of the first neighbour cation increases and when the cation–O_2^- distance decreases [32]. Consequently we may tentatively attribute H_a, H_b and H_c centres to O_2^- ions close to Ba^{2+}, Al^{3+} and Ti^{4+} ions, respectively.

4.2. Simulation of E_2 and E_1 centres

As shown by its g factors, which satisfies $g < g_e$, the E_2 centre can be attributed to Ti^{3+} ions in a distorted environment despite the atypical shape of its EPR powder spectrum, which consists in the association of a narrow and a very broad component. However, the spectrum can be accurately simulated in axial symmetry with $g_\parallel = 1.965$ and $g_\perp = 1.898$ with very anisotropic linewidths $\Delta B_\parallel = 1.5$ mT and $\Delta B_\perp = 7$ mT, as shown in figure 5(a), representing the experimental and simulated spectra of the E_2 centre at 70 K. However, the determination of the orientation of g-tensor axes is difficult to determine from powder spectra. Generally, this information is obtained from single crystal experiments. Fortunately, E_2 centres were also produced by electron irradiation of single crystals of hollandite, as shown in figure 6. This figure shows the EPR spectrum at 70 K of an irradiated single crystal recorded with the

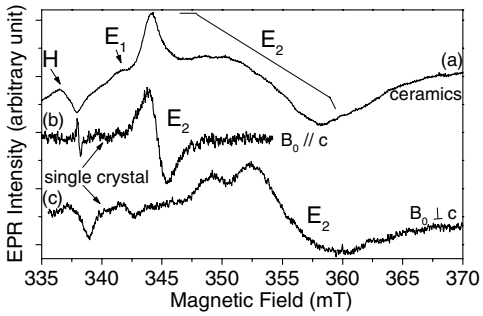

Figure 6. EPR spectra at 70 K of ceramics and single crystals irradiated by 1.5 MeV electrons at a fluence of 5.8×10^{18} cm^{-2}.

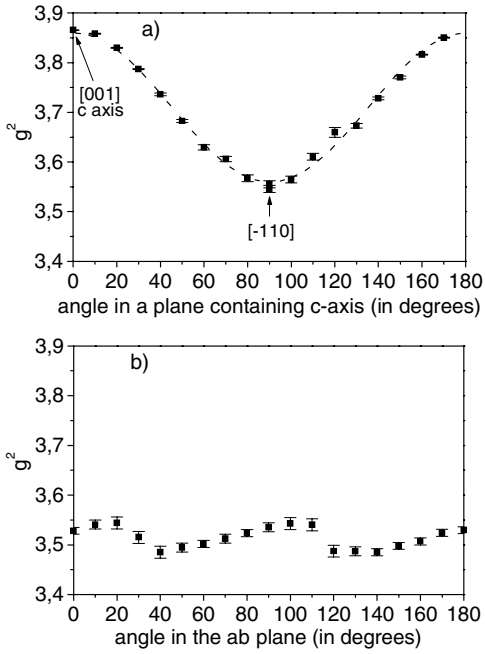

Figure 7. Angular variations of g^2 of the E_2 signal on a single crystal irradiated by 1.5 MeV electrons at a fluence of 5.8×10^{18} cm^{-2}, in a plane containing the **c**-axis (a) and in a plane perpendicular to the **c**-axis (b).

magnetic field parallel and perpendicular to the **c**-axis of the crystal, compared with the EPR spectrum of a hollandite ceramic irradiated under the same conditions (1.5 MeV electrons with 5.8×10^{18} cm^{-2} fluence). The single crystal spectrum clearly shows a narrow symmetrical line at $g = 1.965$ and $\Delta B = 1.9$ mT, corresponding to the parallel component of the powder spectrum, and a broad asymmetric line at $g \approx 1.88$ and $\Delta B \approx 4.8$ mT for $\mathbf{B}_0 \perp \mathbf{c}$. The axial symmetry of this defect is demonstrated by the angular variation of g^2 in a plane containing **c** and the plane perpendicular to **c** (figure 7). The small oscillations of g^2 in the **ab** plane (figure 7(b)), corresponding to extreme g values $g = 1.86(7)$ and $g = 1.88(2)$, indicate a small deviation of the g tensor from the axial symmetry. It appears clearly (table 1) that the g factors measured for single crystals correspond to those deduced from the simulation of the

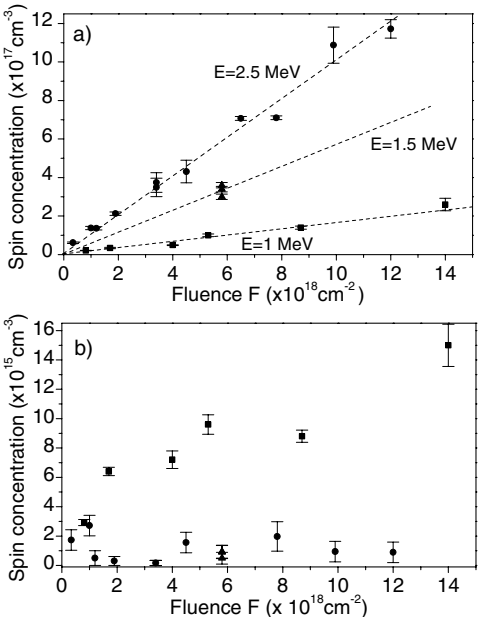

Figure 8. Spin concentration versus fluence at different electron energy ($E = 2.5$ (●), 1.5 (▲) and 1.0 (■) MeV) for (a) E_2 centres and (b) E_1 centres. The slopes σ_p of the lines represent the cross sections of production of E_2 centres.

spectrum of ceramics, except a difference of $\Delta g \approx 0.01$ for the perpendicular component. It can be concluded from single crystal studies that the axial component of the crystal field of the E_2 centre is parallel to the crystallographic axis **c**.

The signal of E_1 centre is more difficult to simulate because it exhibits only a distorted lineshape with no visible structure. We found two sets of g factors which accurately simulate the experimental spectrum (figure 5(b) and table 1). Both are compatible with a Ti^{3+} ion. These two simulations (SA and SB, table 1) indicate a low symmetry of the Ti^{3+} site; however, the two sets of g values are significantly different, so that g factors cannot be used to identify the structure of the E_1 centre. Unfortunately, this signal could not be unambiguously studied with single crystals because of its low intensity compared to that of the E_2 centre, so that it was not possible to identify the direction of the main crystal field component of the E_1 centre.

4.3. Origin of E_2 and E_1 centres

The mechanism at the origin of the two Ti^{3+} centres E_1 and E_2 can be approached by studying the influence of the electron energy on the defect concentrations. The latter have been measured by double integration of the simulated spectra of E_1 and E_2 signals. Figure 8(a) shows the variation of the concentration of E_2 centres versus electron fluence at different electron energies. Such measurements were not interpretable for H centres because the spin concentration was affected by a strong uncertainty induced by the baseline subtraction. It appears that the concentration of E_2 depends linearly on the fluence, with a slope which increases with electron energy (figure 8(a)). The slope represents the cross section for defect production σ_p, which can give information on the nature of the atoms displaced by ballistic collisions. The slope ratios $\sigma_p(1.5\ \text{MeV})/\sigma_p(1\ \text{MeV}) \approx 3.5$ and $\sigma_p(2.5\ \text{MeV})/\sigma_p(1\ \text{MeV}) \approx 6.2$ can be deduced from figure 8(a) for the E_2 centre, which can be compared with the corresponding ratios of

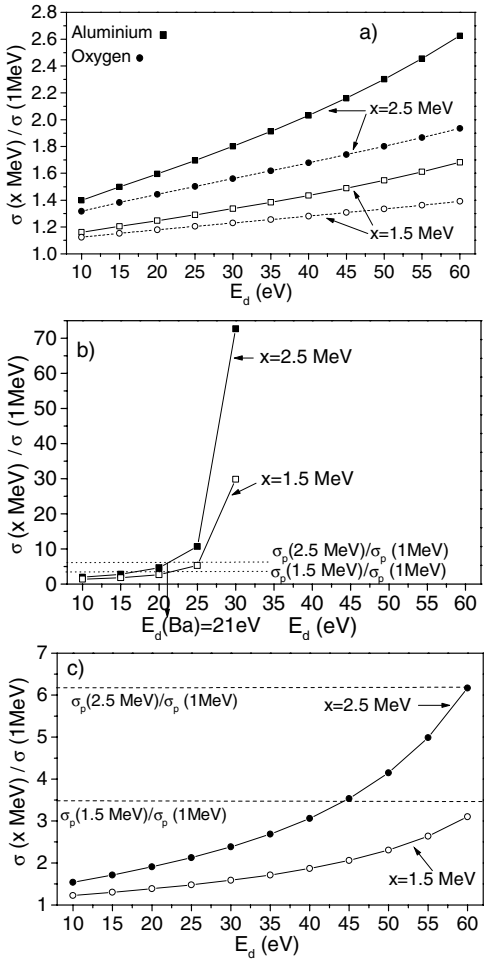

Figure 9. Calculated ratios $\sigma(x\ \text{MeV})/\sigma(1\ \text{MeV})$ ($x = 1.5$ or 2.5 in open or full symbols respectively) of the atomic displacement cross sections versus the displacement energy E_d. (a) Aluminium and oxygen, (b) barium and (c) titanium. The experimental ratios of the cross sections for E_2 centre production $\sigma_\text{p}(x\ \text{MeV})/\sigma_\text{p}(1\ \text{MeV})$ are shown by dashed lines.

the atomic displacement cross-sections by elastic collisions $\sigma(x\ \text{MeV})/\sigma(1\ \text{MeV})$ calculated by using the displacement energy threshold E_d of the different elements (O, Al, Ti, Ba) of hollandite. Figure 9 shows the values of these ratios calculated as a function of E_d with the computer code developed by Lesueur *et al* [23, 24], in the case of Al/O atoms (figure 9(a)), Ba atoms (figure 9(b)) and Ti atoms (figure 9(c)). Owing to the relative dispersion of E_d values found in the literature for the same element (for example see [33–38] for oxygen), which can be understood by the fact that E_d also depends on the crystallographic structure of the material and on the crystal orientation with respect to incident electrons, we chose to perform calculations with E_d in the range 20–60 eV for both oxygen and cations. Figure 9(a) shows that for $E_\text{d} = 60$ eV the ratio $\sigma(x\ \text{MeV})/\sigma(1\ \text{MeV})$ calculated for $x = 2.5$ MeV does not exceed 2.6 and 1.9 for Al and O, respectively, while for $x = 1.5$ MeV this ratio does not exceed 1.6 and 1.4 for these two elements. These calculated values are much smaller than the experimental values 6.2 and 3.5 for $x = 2.5$ and 1.5 MeV, respectively, which clearly exclude displacement

of O and Al as the origin of the E_2 centre. In contrast, calculations of figures 9(b) and (c) show that displacements of Ti and Ba atoms are compatible with the experimental values found for the E_2 centre, since $\sigma(x\ \text{MeV})/\sigma(1\ \text{MeV})$ increases very rapidly with E_d for both atoms. A detailed comparison of calculated and experimental values of $\sigma(x\ \text{MeV})/\sigma(1\ \text{MeV})$ shows that they are compatible with a displacement of Ba with $E_d(\text{Ba}) = 21$ eV. Displacements of Ti atoms also give a good agreement by using $E_d(\text{Ti}) \approx 60$ eV. However, the E_2 centre probably originates from displacement of Ba rather than Ti atoms, as revealed by the slight structural modifications identified by x-ray diffraction (XRD), high resolution transmission electron microscopy (HRTEM) and electron diffraction. In hollandite ceramics irradiated by 1.5 MeV electrons (fluence 5.8×10^{18} cm^{-2}), XRD shows only a broadening of diffraction peaks without observable shift of these peaks. The broadening ranges between 1 and 45% depending on the diffraction peak. These features show that irradiation induces only a structural disorder, with no significant modification of the lattice parameters. More information on this structural disorder is obtained from electron diffraction diagrams. They show a decrease of the diffuse scattering traces indicating that the 1D ordering of Ba^{2+} ions in tunnels is affected, and HRTEM images show the disappearance of the small ordered domains existing before irradiation. This study is currently in progress. However, the preliminary results indicate that disorder in tunnels is due to displacement of Ba ions by elastic collisions, which agrees with the electron-energy dependence of σ_p.

The variation of concentration of E_1 centres versus the electron fluence at the various electron energies (figure 8(b)) is more difficult to interpret. However, we can clearly exclude displacement of heavy atoms (Ba, Ti), and displacements of oxygen or aluminium can be considered. The existence of oxygen displacement by electron irradiation is however clearly demonstrated by solid state NMR, as shown below. Figure 10(a) shows the ^{27}Al MAS-NMR spectra for the pristine sample (black spectrum) and samples irradiated by 1.0 MeV electrons (red spectrum) and 1.5 MeV electrons (blue spectrum). The observed range of chemical shift is typical of Al in an octahedral environment (referred to as Al(VI)) and these spectra cannot be fitted using a single site subjected to a second order quadrupolar interaction broadening. Consequently, a more advanced high-resolution technique, MQMAS (multiple quantum MAS) [39], has been used to obtain more detailed information. Triple quantum MQMAS of the pristine sample is displayed in figure 11(a). The projection of the two-dimensional MQMAS spectra on one dimension, denoted the isotropic dimension, gives a spectrum free of second order quadrupole broadening. As shown by figure 11(c), at least three components are required to correctly reproduce the experimental data, including a broadening which reflects the distribution of environment of Al. Here, a fitting procedure of the MQMAS data including the distribution of NMR parameters (isotropic chemical shift and quadrupole interaction) has been developed. Using a Gaussian distribution for the isotropic chemical shift and a more complex form for the quadrupole interaction (Gaussian isotropic model, see [40, 41]), the MQMAS spectra can be accurately fitted as shown in figure 11(b). This procedure, similar to the MQMAS inversion procedure [42], is out of the scope of the present work and will be described elsewhere [43]. Obtained values of isotropic chemical shifts are typical of hexacoordinated aluminium (Al(VI)), and quadrupole coupling constants are relatively large, in agreement with the strong distortion of the Al octahedra (see table 2). These sites can be assigned according to the occupancy of the three nearest A cation sites in tunnels. NMR data show that the irradiation produces small modifications of these different populations, in agreement with Ba^{2+} ion displacements.

Examination of the wings of the MAS spectra at high magnification (figure 10(b)) also shows the appearance of a weak signal around +45 ppm in irradiated samples, corresponding to the chemical shift of pentacoordinated Al (referred to as Al(V)). Spectra recorded at different

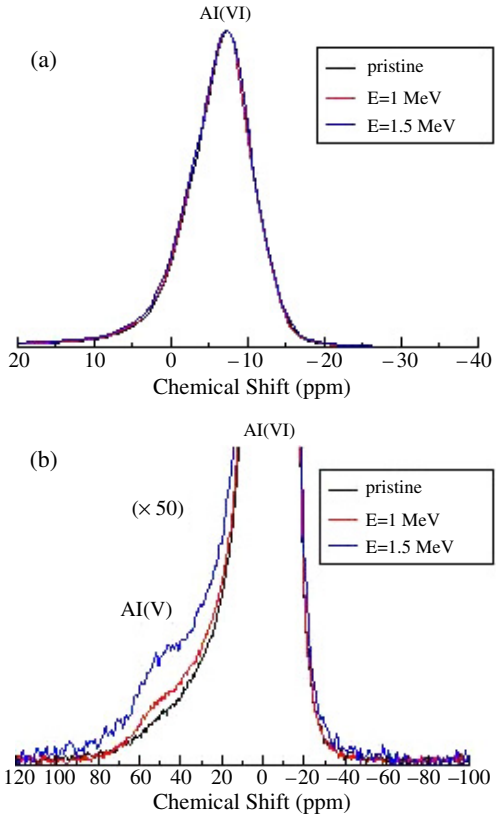

Figure 10. ^{27}Al MAS-NMR spectra of samples before (black spectra) and after irradiation by 1.0 MeV electrons at a fluence of 8.7×10^{18} cm^{-2} (red spectra) or by 1.5 MeV electrons at a fluence of 5.8×10^{18} cm^{-2} (blue spectra). (a) general view of the spectra of hexacoordinated aluminium Al(VI); (b) extended and magnified view of the spectra showing the presence of pentacoordinated aluminium Al(V).

recycle delays (0.25 and 32 s) show similar variations of the Al(VI) lines and the Al(V) satellite, which indicate that the Al(V) line belongs to the hollandite structure and not to a parasitic phase. These sites are too weak to be detected by MQMAS NMR. However, it can be safely concluded from this NMR investigation that oxygen vacancies are produced by electron irradiation.

It thus appears from EPR, NMR, HRTEM and electron diffraction data that electron irradiation mainly produces displacements of barium (for the E_2 centre) and oxygen (for the E_1 centre) as well as electronic excitations.

4.4. Structure of E_2 and E_1 centres

In principle, analysis of the *g* factor of a transition metal ion gives information on the symmetry of metallic sites and the eventual presence of neighbouring defects. This analysis is however not possible for the E_1 centre because we ignore the direction of the *g*-tensor axes and because at least two different sets of *g*-factors accurately simulate its EPR spectrum. For this reason we have used other parameters to obtain information on the environment of Ti^{3+} ions in E_1 and E_2 centres.

It has been indicated in section 3.2 that the spectrum of the E_2 centre vanishes above 140–170 K, so that only the E_1 centre is observable at higher temperature. This indicates that

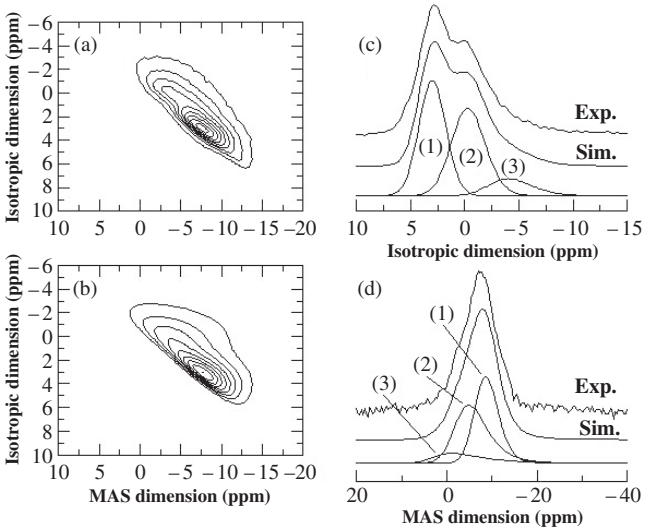

Figure 11. (a) Experimental and (b) simulated ^{27}Al triple quantum MQMAS of the pristine sample, and (d) their projections along the MAS dimension (giving the spectrum as detected in simple MAS experiment) and (c) along the isotropic dimension (dimension free of second order quadrupolar broadening).

Table 2. NMR parameters extracted from MQMAS data (figure 11).

Site	Cq (MHz)	nq	δ_{iso} (ppm)	$\sigma(\delta_{iso})$ (ppm)	Pristine (%)	1 MeV (%)	1.5 MeV (%)
Al(1)	2.3	0.6	−6.7	2.2	39	39.7	40.8
Al(2)	3.3	0.6	−1.8	2.5	45.4	45.3	46.5
Al(3)	4.6	0.6	3.5	2.6	15.6	15	12.7

the spin–lattice relaxation time T_1 of the E_2 centre is smaller than that of the E_1 centre at high temperature, the E_2 spectrum being broadened to something like $\delta(\Delta E) \approx \hbar/T_1$, where $\delta(\Delta E)$ is the EPR linewidth expressed in energy units. In contrast, the spectrum of the E_2 centre is more easily saturated than the E_1 centre at low temperature, which indicates a larger T_1 for the E_2 centre. The influence of the site symmetry of Ti^{3+} ions on their relaxation times can be understood by considering the structure of the Al, Ti sites (figure 1(b)) and the position of the energy levels of Ti^{3+} ions with respect to the band energy levels of hollandite (figure 12).

Owing to the fact that E_1 and E_2 centres originate from oxygen and barium displacements, it is reasonable to assume that these two centres correspond to electrons trapped by Ti^{4+} ions in normal Al/Ti crystallographic sites, stabilized by a positively charged defect in the first or second neighbour position. EHTB band structure calculations show that the electronic structure of hollandite is determined, as for the rutile structure, by the electronic structure of TiO_6 octahedra. The main characteristics of the valence band (VB) and conduction band (CB) can be summarized as follows (figure 12):

(i) the VB is mainly of O(2p) character, and represents bonding Ti–O interactions;
(ii) the top of the VB is of antibonding O–O character and of non-bonding Ti–O character;
(iii) the CB is mainly Ti–O antibonding and of Ti(3d) character; it reflects the splitting of Ti(3d) orbitals into t_{2g} and e_g sets by the octahedral crystal field, the t_{2g} set forming the bottom of the CB;

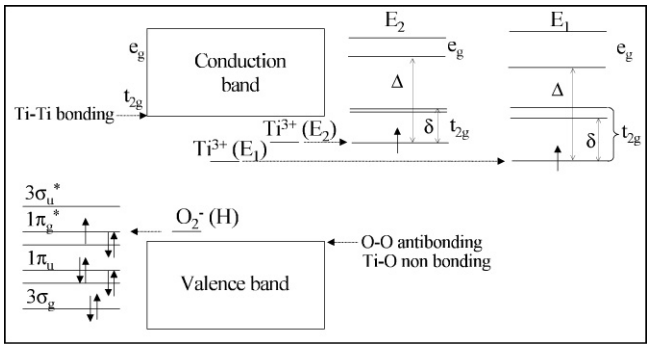

Figure 12. Schematic energy levels of the irradiation-induced centres H, E_1 and E_2 with respect to the hollandite band structure.

(iv) as TiO_6 octahedra share edges along the *c*-axis, the band structure shows a significant dispersion along this axis, due to bonding Ti–Ti interactions between t_{2g} orbitals across the edge (see figure 1(b)).

The low symmetry of TiO_6 octahedra splits the t_{2g} orbital set by an energy δ (figure 12), so that the bottom of the CB is made from the low energy part of the split t_{2g} manifold. Thus any positively charged point defect close to a TiO_6 site will increase the splitting δ and lower its ground state t_{2g} orbital, which thus forms an electron trap level in the bandgap. The two centres E_1 and E_2 differ by the nature and the position of the neighbouring defects, which control the splitting δ and thus the depth of the electron trap in the bandgap. The amplitude of this splitting is determined by the charge of the defect and its position with respect to the Ti site, a defect in the first neighbour position (O) inducing a larger δ than a defect in the second neighbour position (Ba).

The comparison of E_1 and E_2 centres with respect to their splitting δ can be made from the temperature dependence of the relaxation time T_1 via the lifetime broadening effect at high temperature (short T_1) and the saturability at low temperature (long T_1). It is well established that the relaxation rate $1/T_1$ of transition metal ions with d^1 configuration is largely influenced by the splitting δ of the t_{2g} level [44]:

$$\frac{1}{T_1} = aT + bT^n + c\delta^3 \exp\left(\frac{-\delta}{kT}\right) \tag{4}$$

where the first term aT represents the one-phonon direct process, the second term bT^n (with $n = 7$ or 9) represents the two-phonon Raman process and the exponential term represents the Orbach process. It appears evident from equation (4) that the Orbach term will dominate the relaxation rate for small splitting δ. The fact that the E_2 centre vanishes by the lifetime broadening at relatively low temperature (140–170 K) indicates that the δ of this centre is smaller than that of the E_1 centre. A large splitting is expected for an oxygen vacancy in a TiO_6 unit, giving a TiO_5 group, while a smaller splitting is expected for an extra Ba^{2+} ion close to a TiO_6 unit (see figure 1(b)). We may thus attribute the E_1 centre to an electron trapped by a Ti^{4+} ion adjacent to an oxygen vacancy, and the E_2 centre to an electron trapped by a Ti^{4+} ion close to an extra Ba^{2+} ion in a neighbouring tunnel site. The position of the energy levels of E_1, E_2 and H centres with respect to CB and VB extrema are represented in figure 12. The two Ti^{3+} centres E_1 and E_2 form two localized levels below the bottom of the CB (electron traps), while the H centre (superoxide ion O_2^-) being of O(2p) character forms a level above the top of the

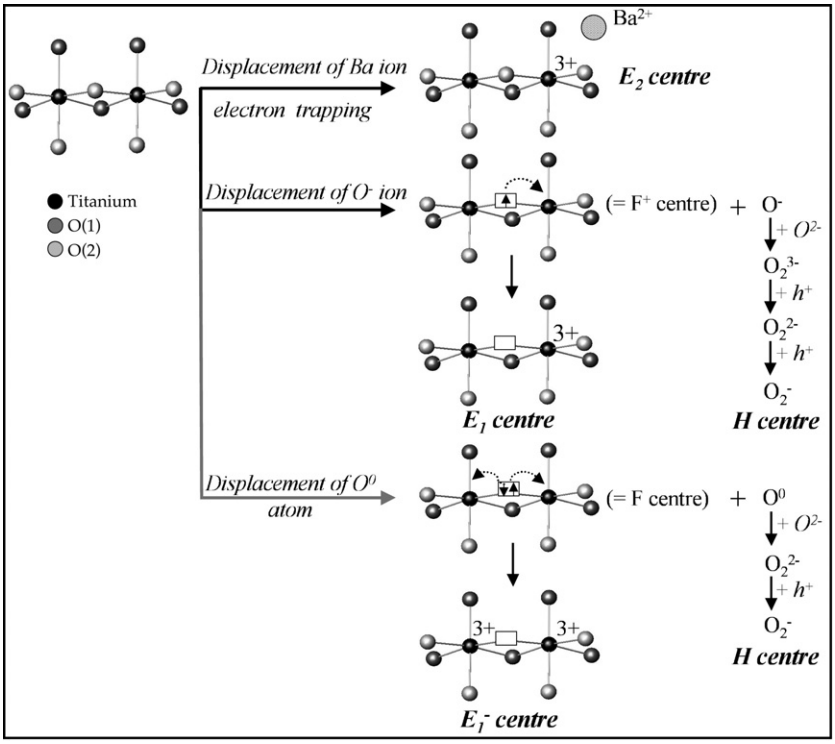

Figure 13. Proposed mechanism for the formation of H, E_1 and E_2 centres by electron irradiation.

VB (hole trap). Indeed, the electronic configuration of O_2^- being $(1\pi_u)^4(1\pi_g^*)^3$, the H centre may be described as a hole trapped in an antibonding π_g orbital of a O–O pair.

5. Mechanism of defect creation

A mechanism of formation of E_1, E_2 and H centres based on electron–hole creation and displacement of Ba and O ions can be proposed on the basis of all the observations of the present work. Figure 13 represents a model for the evolution upon irradiation of two edge-shared Ti sites, forming a Ti_2O_{10} group. The E_2 centres may be simply explained by the trapping of an electron by a Ti^{4+} ion in the nearest neighbour position of an extra Ba^{2+} ion displaced by ballistic collision (top of figure 13).

E_1 and H centres may result from the displacement of oxygen by electron irradiation. The crystal field created by the oxygen vacancy increases the splitting δ of the t_{2g} levels of Ti^{4+} adjacent to the vacancy, creating an electron trap level in the gap (figure 12). Two cases can be considered depending on the charge state of the displaced oxygen. If the oxygen is displaced in the form of an O^- ion (middle of figure 13), the oxygen vacancy is compensated by one electron and corresponds to the standard F^+ centre of oxides [28]. However, owing to the metal 3d character of the electronic level formed in the gap, the unpaired electron of the F^+ centre is localized in the ground state t_{2g} orbital of the Ti^{4+} ion adjacent to the vacancy, which is the E_1 centre (middle of figure 13). The displaced O^- ion is hereafter associated with an O^{2-} ion of the structure, forming an O_2^{3-} ion. As this ion pair has the $(1\pi_g^*)^4(3\sigma_u^*)^1$ configuration, it can be described as a hole localized in an antibonding σ_u^* orbital of an oxygen pair, which

shortens the O–O distance with respect to the normal distance between two adjacent O^{2-} ions of the structure. This O–O bond shortening shifts the antibonding levels above the top of the VB. It is important to note, however, that O_2^{3-} does not correspond to the H centre (see section 4.1). The negative charge of O_2^{3-} (resulting from an interstitial O^- ion) makes this pair a hole trap according to the following reaction (figure 13):

$$O^- + O^{2-} \xrightarrow{h^+} O_2^{2-} (\equiv H^- \text{centre}). \tag{5}$$

The diamagnetic pair O_2^{2-} having the configuration $(1\pi_g^*)^4(3\sigma_u^*)^0$ with an empty antibonding σ_u^* orbital, its O–O bond length is shorter than in the O_2^{3-} pair. This further destabilizes the antibonding π_g^* orbital, which forms a hole trap level above the top of the VB. Thus we suggest that the O_2^{2-} ion can trap another hole giving a superoxide O_2^- ion (figure 12):

$$O_2^{2-} + h^+ \rightarrow O_2^- (\equiv \text{Hcentre}). \tag{6}$$

Alternatively, if the oxygen is displaced in the form of a neutral O^0 atom, it leaves a neutral oxygen vacancy compensated by two electrons (an F centre) and forms an O_2^{2-} pair by association with an O^{2-} ion of the structure. The latter gives an H centre by hole trapping:

$$O^0 + O^{2-} \rightarrow O_2^{2-} (\equiv H^- \text{centre}) \xrightarrow{h^+} O_2^- (\equiv \text{Hcentre}). \tag{7}$$

This type of mechanism based on a cascade of hole trapping by interstitial oxygen could be involved in the formation of oxygen bubbles found in nuclear waste glasses [45, 46], the O_2^- ion constituting the ultimate step before molecular oxygen formation by hole trapping.

However, according to the above considerations on the structure of electron traps in hollandite, the two electrons of the F centre should be localized in ground state t_{2g} orbitals of Ti^{4+} ions adjacent to the oxygen vacancy. The corresponding defect is better described as a Ti^{3+}–V_O–Ti^{3+} cluster (V_O being the oxygen vacancy). This defect can be considered as the negative analogue of the E_1 centre (E_1^- centre). The Ti^{3+}–V_O–Ti^{3+} cluster being formed by two adjacent paramagnetic Ti^{3+} ions with spin $S = 1/2$, the ion pair can exhibit either a $S = 1$ spin if the exchange interaction between Ti^{3+} ions is of the ferromagnetic type (through space direct Ti–Ti interaction), or an $S = 0$ spin if the exchange interaction is of the antiferromagnetic type (through-bond Ti–O–Ti superexchange interaction). As we did not detect any EPR signal indicating a triplet state $S = 1$, and according to the fact that exchange interaction between two transition metal ions linked by an oxygen bridge is dominated by superexchange interactions [44], we thus expect that the Ti^{3+}–V_O–Ti^{3+} defect should be diamagnetic ($S = 0$).

The proposed mechanism implies that the defects induced by barium and oxygen displacements followed by electron and hole trapping are of two types: (i) oxygen centres which can be paramagnetic (O_2^-, or H centre) or diamagnetic (O_2^{2-} or H^- centre), and (ii) Ti^{3+} centres which can be paramagnetic (E_2 and E_1 centres) or diamagnetic (E_1^- centre). It is evident that we can only suggest the existence of these diamagnetic centres.

6. Discussion and conclusion

We discuss in this section the significance of external electron irradiation experiments with respect to actual conditions in hollandite storage waste forms. We have shown that the same types of E_1, E_2 and H centres are always produced whatever the conditions of electron energy and fluence. A maximum defect concentration of the order of 10^{18} cm^{-3} was obtained with our irradiation conditions; however, the total concentration can be higher if diamagnetic defects are also produced. These diamagnetic defects can be either the diamagnetic counterparts of E_1, E_2 and H centres, or also diamagnetic defects that have no paramagnetic counterparts.

It is thus expected that the same types of defects would be produced by the β^- emission by radioactive caesium during storage. The maximum absorbed dose (7.5×10^9 Gy) in our experiments corresponds to the first 30 years of Cs storage when 5 wt% of Cs_2O is incorporated in the hollandite structure, and to 40% of the total absorbed dose during the whole storage time. The electron dose rates (26×10^6 to 75×10^6 Gy h^{-1}) used in our experiments are relatively high in comparison with that occurring during the storage in hollandite waste forms. The actual dose rate would decrease from 10^5 Gy h^{-1} at the beginning of storage to 3×10^3 Gy h^{-1} after one century. It is to be noted, however, that the dose rate conditions remained about 4–5 orders of magnitude lower in our study than in transmission electron microscopes [13, 14]. Thus our experimental conditions are closer to the storage conditions than conditions occurring in electron microscopes. The electron energies (1.0, 1.5 and 2.5 MeV) used in this work were higher than the energies of several types of β-particles in hollandite waste forms: 0.514 and 1.176 MeV for ^{137}Cs (43% of the caesium), 0.205 MeV for ^{135}Cs (12% of the caesium), 0.089 to 1.454 MeV for ^{134}Cs (about 1% of the caesium). The low energy of β-particles implies that the electron irradiation conditions in the present work overestimate the effect of ballistic collisions, and in particular the displacements of Ba^{2+} ions will be much less frequent in real storage conditions. We thus expect a smaller E_2/E_1 ratio in waste forms than in the present work. However, E_2 centres may also form by electron trapping by Ti^{3+} ions adjacent to pre-existing positive charge excess due to extra Ba^{2+} ions. In contrast, β-decay will be efficient to produce oxygen displacements and electronic excitations, so we expect important quantities of E_1 and H centres.

It is important to note that two important differences exist between our experimental conditions and the actual conditions in waste forms. First, electrons fly through the sample to avoid charge accumulation in the sample for external irradiation conditions, and thus electrons are not finally trapped by the hollandite host. Consequently, these experiments reproduce only the effect of β-particles and Compton electrons (produced by γ-rays) emitted by Cs along their path in the hollandite structure, and do not simulate the effect of electron capture. Secondly, all our experiments were performed at room temperature. However, because of the high thermal power of ^{137}Cs and ^{134}Cs isotopes, the temperature in the bulk of hollandite ceramics could reach 300 °C during the first years of storage for a 5 wt% loading of Cs_2O. A first effect of the high temperature could be to favour the displacement of Ba^{2+} ions in the tunnels of hollandite, and thus to favour the formation of E_2 centres during β-irradiation. The most probable effect of temperature could be the migration of oxygen vacancies and interstitial oxygen. We thus expect an evolution of E_1 and H centres at high temperature, which may either recombine and annihilate, or convert into more stable defects. The study of thermal stability of E_2, E_1 and H centres is thus of fundamental interest.

Acknowledgments

This work was supported by the *Commissariat à l'Energie Atomique* (CEA), Marcoule, France. We thank particularly Dr Thierry Advocat for helpful discussions. The authors also thank the *Région Ile-de-France* for financial support (grant No E1663).

References

[1] Madic C, Lecomte M, Baron P and Boullis B 2002 *C.R. Physique* **3** 797
[2] Fillet C, Advocat T, Bart F, Leturcq G and Rabiller H 2004 *C.R. Chimie* **7** 1165
[3] Browne E, Dairiki J M and Doebler R E 1978 *Table of Isotopes* 7th edn, ed C M Lederer and V S Shirley (New York: Wiley)

[4] Lide D R 1997 *Handbook of Chemistry and Physics* 78th edn (Boca Raton, FL: Chemical Rubber Company Press)
[5] Bursill L A 1987 *J. Solid State Chem.* **69** 355
[6] Bursill L A 1979 *Acta Crystallogr.* B **35** 530
[7] Cheary R W 1996 *Mater. Sci. Forum* **228** 777
[8] Cheary R W, Thompson R and Watson P 1988 *Mater. Sci. Forum* **27/28** 397
[9] Kesson S E and White T J 1986 *Proc. R. Soc.* A **408** 295
[10] Bursill L A and Smith D J 1987 *J. Solid State Chem.* **69** 343
[11] Fielding P E and White T J 1987 *J. Mater. Res.* **2** 387
[12] Weber W J 1985 *Mater. Res. Soc. Symp. Proc.* **44** 671
[13] Ball C J and Woolfrey J L 1983 *J. Nucl. Mater.* **118** 159
[14] Barry J C, Hutchinson J L and Segall R L 1983 *J. Mater. Sci.* **18** 1421
[15] Roth R S, Brower W S, Austin M and Koob M 1981 *Annual Reports, National Measurement Laboratory, Office of Measurements for Nuclear Technology* NBSIR 81-2241
[16] Aubin V, Caurant D, Gourier D, Baffier N, Advocat T, Bart F, Leturcq G and Costantini J M 2004 *Mater. Res. Soc. Symp. Proc.* **807** 315
[17] Aubin-Chevaldonnet V 2004 *PhD Thesis* Université Pierre et Marie Curie, Paris, France
[18] Kesson S E and White T J 1986 *Proc. R. Soc.* A **405** 73
[19] Bart F, Leturcq G and Rabiller H 2004 *Environmental Issues and Waste Management Technologies in the Ceramic and Nuclear Industries* vol IX, ed J D Vierra and D R Spearing; *Ceram. Trans.* **155** 11
[20] Aubin V, Caurant D, Gourier D, Baffier N, Esnouf S and Advocat T 2004 *Mater. Res. Soc. Symp. Proc.* **792** 61
[21] Knoll G F 2000 *Radiation Detection and Measurement* (New York: Wiley)
[22] PENELOPE http://www.nea.fr/html/dbprog/penelope.pdf
[23] Dunlop A, Lesueur D and Dural J 1989 *Nucl. Instrum. Methods* B **42** 182
[24] Lesueur D, Morillo J, Mutka H, Audouard A and Jousset J C 1983 *Radiat Eff.* **77** 125
[25] Amoureux J P, Fernandez C and Steuernagel S 1996 *J. Magn. Reson.* **123** 16
[26] Thorp J S and Eggleston H S 1985 *J. Mater. Sci.* **4** 1140
[27] De Biasi R S 1996 *J. Phys. Chem. Solids* **57** 137
[28] Henderson B and Wertz J E 1977 *Defects in the Alkaline Earth Oxides* (London: Taylor and Francis)
[29] Gourier D, Vivien D and Livage J 1979 *Phys. Status Solidi* a **56** 247
[30] Lundsford J H and Jayne J P 1966 *J. Chem. Phys.* **44** 1487
[31] Naccache C, Meriaudeau P, Che M and Tench A J 1971 *Trans. Faraday Soc.* **67** 506
[32] Murphy D M, Griffiths E W and Roxlands C C 1997 *Chem. Commun.* 2177
[33] Buck E C 1995 *Radiat. Eff. Defects Solids* **133** 141
[34] Smith K L, Cooper R, Colella M and Vance E R 2001 *Mater. Res. Soc. Symp. Proc.* **663** 373
[35] Weber W J, Ewing R C and Catlow C R A 1998 *J. Mater. Res.* **13** 1434
[36] Zincle S J and Kinoshita C 1997 *J. Nucl. Mater.* **251** 200
[37] Perez A and Mc Hargue J C 1993 *Solid State Phenom.* **30/31** 297
[38] Balanzat E and Bouffard S 1993 *Solid State Phenom.* A **32** 751
[39] Frydman L and Harwood J S 1995 *J. Am. Chem. Soc.* **5367** 117
[40] Le Caër G and Brand R A 1998 *J. Phys.: Condens. Matter* **10** 10715–74
[41] Czjzek G, Fink J, Götz F, Schmidt H, Coey J M D, Rebouillat J P and Liénard A 1981 *Phys. Rev.* B **23** 2513–30
[42] Angeli F, Charpentier T, Faucon P and Petit J C 1999 *J. Phys. Chem.* B **103** 10356
[43] Charpentier T, Aubin V, Caurant D and Gourier D 2006 in preparation
[44] Pilbrow J R 1990 *Transition Ion Electron Paramagnetic Resonance* (Oxford: Clarendon)
[45] Weber W J, Ewing R C, Angell C A, Arnold G W, Cormack A N, Delaye J M, Griscom D L, Hobbs L W, Navrotski A, Price D L, Stoneham A M and Weinberg W C 1997 *J. Mater. Res.* **12** 1946
[46] Boizot B, Petite G, Ghaleb D, Reynard B and Calas G 1999 *J. Non-Cryst. Solids* **243** 268